5372 *Macromolecules* **2009**, *42*, 5372–5377
DOI: 10.1021/ma900426v

Macromolecules
ARTICLE

Loss Amplification Effect in Multiphase Materials with Viscoelastic Interfaces

Andrei A. Gusev*[,†] **and Sergey A. Lurie**[‡]

[†]*Institute of Polymers, Department of Materials, ETH Zürich, 8093 Zürich, Switzerland, and* [‡]*Institute of Applied Mechanics, The Russian Academy of Sciences, 117334 Moscow, Russia*

Received February 25, 2009; Revised Manuscript Received May 5, 2009

ABSTRACT: A combination of numerical and modeling approaches is employed to study the effective energy dissipation properties of solid polymer matrixes filled with coated spherical inclusions. For the coating layers, typical viscoelastic properties of a polymer at and well above the glass transition region are assumed. It is shown that by optimizing the thickness of the layers, one can achieve multiphase materials with effective loss characteristics significantly exceeding those of the individual material's constituents. Upon varying the layers' thickness, we detect two distinct peaks of energy dissipation. By analyzing spatial distributions of local energy dissipation rates, we relate the origins of the two peaks to two different states of local strain realizable inside the sections of maximum energy dissipation. We surmise that such lossy composites may prove technologically appealing, as one could use conventional polymer-processing equipment to directly process them into lossy complex-shape structural parts.

Introduction

Viscoelastic polymers are widely used for acoustic and vibration damping. Physically, it is the complex shear modulus which is commonly employed to characterize the elastic properties of such materials. At a given angular frequency ω, the complex shear modulus is defined as $\mu = \mu' + i\mu''$, and it is the imaginary part μ'' (also called the loss modulus) which formally defines the rate of energy dissipation per unit volume $\dot{E} = \mu''\gamma_0^2$, where γ_0 is the amplitude of harmonic shear strain applied to a viscoelastic continuum.

The effective loss modulus μ''_{eff} of a two-phase medium is not bound by those of the constituents. For example, let us consider a lamella-morphology setup, see Figure 1. Upon shearing in the xy-plane, the effective complex shear modulus is

$$\frac{1}{\mu_{\text{eff}}} = \frac{f}{\mu_2} + \frac{1-f}{\mu_1} \tag{1}$$

where μ_1 and μ_2 are complex-valued shear moduli of the two layers respectively and f is the volume fraction of the second layer. Suppose now that the first layer is stiff and nonlossy with a shear modulus of $\mu_1 = b$ while the second layer weak and lossy with $\mu_2 = a(1+i\eta)$, where a, b, and η are real-valued parameters. Figure 1 shows that, upon varying f, the effective shear modulus goes through a maximum, reaching values orders of magnitude larger than that of the lossy layer.

By analyzing the asymptotic behavior for $a/b \to 0$, one finds that the maximum occurs at

$$f = \sqrt{1+\eta^2}(a/b) \tag{2}$$

with a maximum value of

$$\mu''_{\text{eff}} = b(\sqrt{1+\eta^2} - 1)/2\eta \tag{3}$$

Surprisingly, the maximum value is independent of the absolute stiffness a of the lossy layer, thus highlighting a remarkable loss-amplification mechanism operative in lamellar systems with viscoelastic interfaces.

One can readily show that eq 1 is also valid for the effective elastic constant C_{eff} describing the overall normal strain responses in the z-direction. Figure 1 shows that similar to the shear loss modulus μ''_{eff}, the C''_{eff} also goes through a maximum but at a different value of f and with a different magnification factor at the maximum. This indicates that one should carefully consider the loading conditions when designing optimal damping solutions for specific applications.

Damping solutions involving lamellar geometries are widely used in practice.[1] For example, it is a commonplace solution to apply a layer of a viscoelastic material to the surface of a vibrating beam or plate. An alternative solution involves a constrained-layer damping treatment where a thin viscoelastic layer applied to the surface of a structure is canned by an additional metal sheet.

In this work, we use a combination of modeling and numerical tools to study composite materials consisting of a matrix filled with spherical inclusions coated with a layer of lossy viscoelastic material. We show that the remarkable loss amplification mechanism is also operative in such particulate−morphology materials.

Time-Domain Finite Element Approach

We use the finite element method to extract the overall, effective properties of composite, multiphase materials from those of the constituent phases and the materials' morphologies, on the basis of periodic multi-inclusion computer models meshed into unstructured morphology-adaptive tetrahedron-based meshes,[2−5] see Figure 2. Perfect adhesion is assumed at all the internal boundaries. For static, zero-frequency elastic, thermal, electric, and transport properties, the approach has already been introduced elsewhere.[2,3] Here we extend the approach to dynamic viscoelastic properties.

---

*Corresponding author.

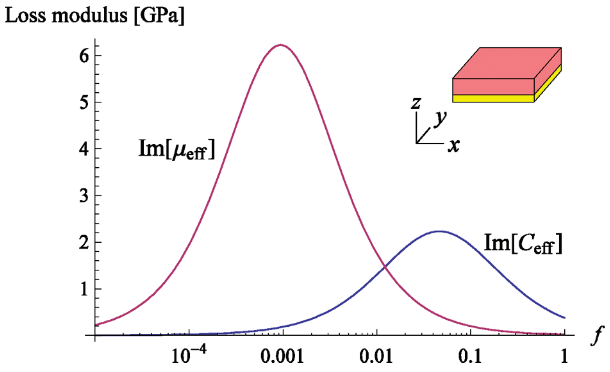

Figure 1. The loss-amplification phenomenon in lamellar media. Periodic boundary conditions are imposed in all three Cartesian directions. In calculations, we assumed $\mu_1 = 30$ GPa and $C_1 = 80$ GPa for the first phase (silica) together with $\mu_2 = 0.02(1 + i)$ GPa and $C_2 = 3.5(1+i0.1)$ GPa for the second phase (a viscoelastic polymer in its glass transition region). Remarkably, the effective shear loss modulus at the maximum is about 300 times larger than that of the viscoelastic polymer.

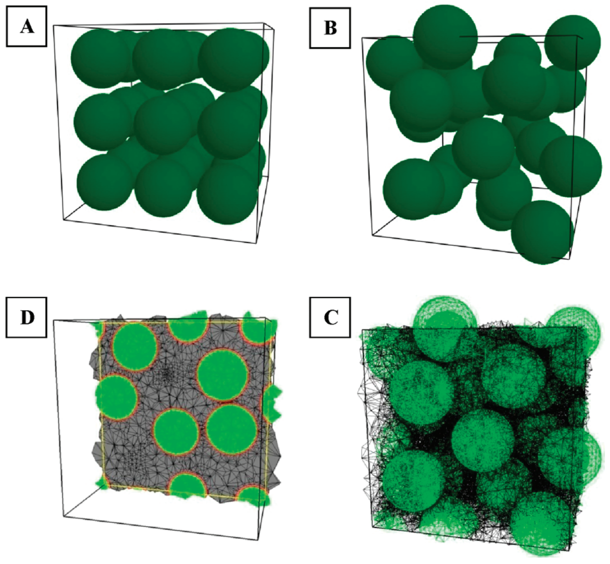

Figure 2. Morphology-adaptive tetrahedron-based meshes. Periodic boundary conditions are employed. **A**. Initial cubic array of 27 spheres. **B**. A random Monte Carlo snapshot with 27 nonoverlapping spheres. **C**. A tetrahedron-based quality mesh. Steps **A**–**C** have already been discussed elsewhere.[2–4] **D**. Introduction of the coating layers. For each inclusion we first duplicate the interfacial nodes. We then use an affine transformation to scale the coordinates of all the inclusion nodes (including the original interfacial nodes) toward the centers of the corresponding inclusions. Obviously, this scaling does not violate the mesh connectivity inside the spheres. We then connect the corresponding initial and duplicated nodes to obtain layers of triangular-base prisms representing the interfacial layers of the spheres. Finally, we divide each prism into three tetrahedrons, see the red sections in part **D**.

Formulation. At a given frequency ω, we use a back-strain form linear constitutive equation

$$\boldsymbol{\sigma} = \mathbf{D}(\boldsymbol{\varepsilon} - \boldsymbol{\varepsilon}_0) + \mathbf{Q}(\dot{\boldsymbol{\varepsilon}} - \dot{\boldsymbol{\varepsilon}}_0) \qquad (4)$$

to relate stress tensor $\boldsymbol{\sigma}$ with strain tensor $\boldsymbol{\varepsilon}$ and strain rate tensor $\dot{\boldsymbol{\varepsilon}}$. Tensors $\mathbf{D}$ and $\mathbf{Q}$ are position-dependent real-valued stiffness and viscosity tensors of the viscoelastic medium under consideration. Tensor $\boldsymbol{\varepsilon}_0$ stands for a back-form time dependent homogeneous deformation applied to the system. Appealingly, as the driving strain $\boldsymbol{\varepsilon}_0$ is applied inside the problem domain, the back-form strain approach can readily be used under periodic boundary conditions.[2,3]

The overall, effective elastic constants are then defined as complex-valued coefficients relating the steady-state harmonic oscillations of the volume-averaged stress $\langle\boldsymbol{\sigma}\rangle$ and applied strain $\boldsymbol{\varepsilon}_0$.

We use the principle of virtual work (or equivalently, a weak form of the equilibrium equations)

$$\int \boldsymbol{\delta\varepsilon}^{\mathrm{T}} \boldsymbol{\sigma}\, \mathrm{d}V = 0 \qquad (5)$$

where the integration is performed over the system volume V. Substituting eq 4 into eq 5, one obtains discrete equations

$$\mathbf{K}\mathbf{a} + \mathbf{C}\dot{\mathbf{a}} = \mathbf{f} \qquad (6)$$

Where $\mathbf{a}$ and $\dot{\mathbf{a}}$ are system displacement and velocity vectors made up of the individual nodal contributions, and

$$\begin{aligned} \mathbf{K} &= \int \mathbf{B}^{\mathrm{T}}\mathbf{D}\mathbf{B}\, \mathrm{d}V \\ \mathbf{C} &= \int \mathbf{B}^{\mathrm{T}}\mathbf{Q}\mathbf{B}\, \mathrm{d}V \\ \mathbf{f} &= \int \mathbf{B}^{\mathrm{T}}(\mathbf{D}\boldsymbol{\varepsilon}_0 + \mathbf{Q}\dot{\boldsymbol{\varepsilon}}_0)\, \mathrm{d}V \end{aligned} \qquad (7)$$

where $\mathbf{B}$ is the element strain–displacement matrix defining a trial strain field via $\boldsymbol{\varepsilon} = \mathbf{B}\mathbf{a}$.[6]

Steady-state method. For a given harmonic perturbation $\mathbf{f} = \mathbf{f}_0 \mathrm{e}^{i\omega t}$, the steady-state displacements are also harmonic functions of time, i.e., $\mathbf{a} = (\mathbf{a}' + i\mathbf{a}'')\mathrm{e}^{i\omega t}$. Inserting this form into eq 6 and rearranging terms gives a multidimensional saddle-point problem

$$\begin{pmatrix} \mathbf{K} & -\omega\mathbf{C} \\ \omega\mathbf{C} & \mathbf{K} \end{pmatrix} \begin{pmatrix} \mathbf{a}' \\ \mathbf{a}'' \end{pmatrix} = \begin{pmatrix} \mathbf{f}_0 \\ 0 \end{pmatrix} \qquad (8)$$

In principle, one can attempt to solve this equation set directly, by using an oblique projection Krylov-subspace solver (for example, GMRES), or a conjugate gradient solver on the normal equations, or by means of Uzawa's iterations.[7] But because of numerical stagnation, neither technique is actually suitable for solving large-scale (with 10^6 and more degrees of freedom) saddle-point problems arising in this work.

Time-Domain Method. Suppose that at time t_n the displacement vector $\mathbf{a}^{(n)}$ and the velocity vector $\dot{\mathbf{a}}^{(n)}$ are known. To obtain a numerical scheme for stepping from time t_n to $t_{n+1} = t_n + \Delta t$, we impose dynamic equilibrium at time t_{n+1}

$$\mathbf{K}\mathbf{a}^{(n+1)} + \mathbf{C}\dot{\mathbf{a}}^{(n+1)} = \mathbf{f}^{(n+1)} \qquad (9)$$

where both vectors $\mathbf{a}$ and $\dot{\mathbf{a}}$ are now real-valued functions of time. By using the trapezoidal ("average velocity") difference formula

$$\dot{\mathbf{a}}^{(n+1)} = \frac{2}{\Delta t}(\mathbf{a}^{(n+1)} - \mathbf{a}^{(n)}) - \dot{\mathbf{a}}^{(n)} \qquad (10)$$

we obtain a Crank–Nicolson type, unconditionally stable algorithm

$$\left(\mathbf{C} + \frac{\Delta t}{2}\mathbf{K}\right)\mathbf{a}^{(n+1)} = \frac{\Delta t}{2}\mathbf{f}^{(n+1)} + \mathbf{C}\left(\mathbf{a}^{(n)} + \frac{\Delta t}{2}\dot{\mathbf{a}}^{(n)}\right) \qquad (11)$$

At each time step, one needs to solve a system of linear equations for the components of $\mathbf{a}^{(n+1)}$. However, because both $\mathbf{K}$ and $\mathbf{C}$ are symmetric positive-definite, the above

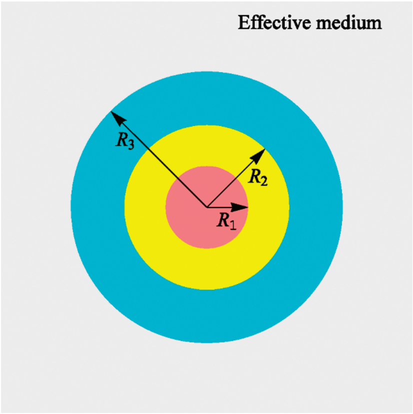

Figure 3. Four-phase composite sphere model. In this work, we define the inclusion (sphere) volume fraction as $f = (R_2/R_3)^3$, thus including the layer's volume in the definition of f.

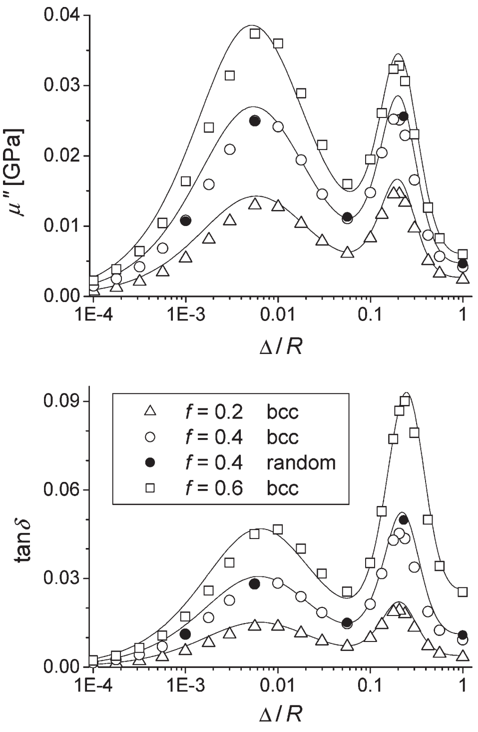

Figure 4. Morphological effects. Open symbols give predictions obtained with a regular bcc model with two spheres per unit cell whereas solid symbols those obtained with a random Monte Carlo snapshot with 27 spheres, see Figure 2B. Solid lines stand for predictions of the four-phase sphere model. The sphere radius R corresponds to R_2 while the layer thickness is defined as $\Delta = R_2 - R_1$; see Figure 3. As for the computer timing, each time-domain finite element prediction with random and bcc structures requires about 3 CPU days and 3 CPU hours on a 1.6 GHz Itanium 2 processor, respectively. This difference is due to the fact that simply geometrically, one should use many more tetrahedral elements to describe a random model with 27 spheres compared to those required for describing a bcc model with 2 spheres. Compared to the direct finite element predictions, the composite-sphere model predictions involve a negligible numerical effort.

equation system is also positive definite. Hence, one can use a preconditioned conjugate gradient solver for updating the displacement vector. And moreover, for sufficiently small Δt vector $\mathbf{a}^{(n)}$ forms excellent initial approximation to $\mathbf{a}^{(n+1)}$, so in practice the convergence of conjugate gradient iterations is relatively fast.

Implementation. In this work, we used cubic polynomial interpolation for the displacements, resulting in 20×20 tetrahedral-element strain−displacement matrices.[6] The computer implementation was validated by reproducing exact analytical solutions available for lamellar morphologies. As initial approximation at $t = 0$, we used $\mathbf{a} = 0$ and $\dot{\mathbf{a}} = 0$. External harmonic strain $\boldsymbol{\varepsilon}_0$ was then applied. The integration time step Δt was chosen to result in 30−50 integration points per period. Typically, a single equilibration cycle was sufficient to bring the system in the steady-state domain. At each integration point, the average system stress was calculated. The resulting stress values were fitted to harmonic functions, which were then used to extract the effective complex-valued elastic constants. For example, for a single-component harmonic shear strain $\varepsilon_0 = \sin \omega t$, the corresponding stress component was fitted to $\sigma = \sigma_0 \sin(\omega t + \delta)$ and the effective shear modulus was obtained as $\mu_{\text{eff}} = \sigma_0\,(1 + i \tan \delta)$.

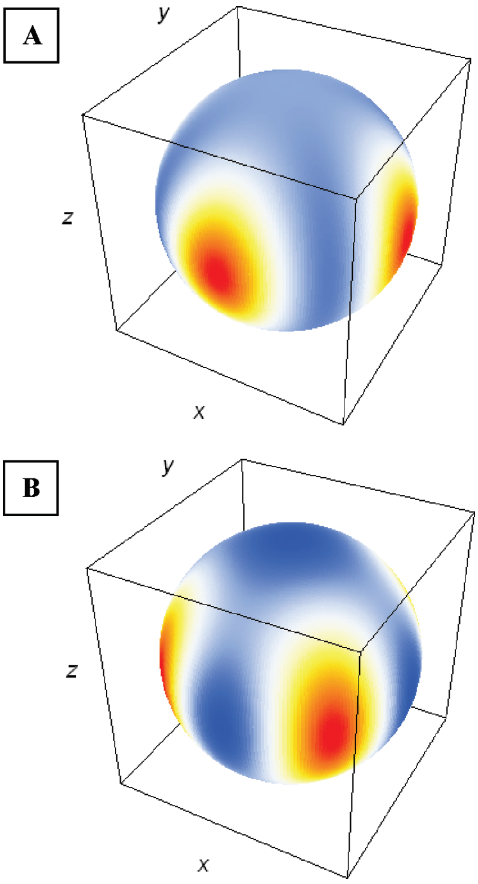

Figure 5. Distributions of local energy dissipation rates at the maxima of the two peaks, see Figure 4. We use the four-phase sphere model to evaluate the underlying displacement fields, and then employ the fields to calculate the local energy dissipation rates. In calculations we assumed $f = 0.4$ and used the same materials properties as in Figure 4. **A**. The first peak at $\Delta/R \approx 0.2$. **B**. The second peak at $\Delta/R \approx 0.007$. In both cases, we have normalized the local dissipation rates by the corresponding maximum values. Red color corresponds to the dimensionless energy-dissipation rate of one whereas blue color to the lowest one.

Four-Phase Composite Sphere Model

Consider a spherical assembly consisting of three concentric spheres embedded in an infinite effective medium, see Figure 3. The inner sphere of radius R_1 represents a spherical inclusion with bulk modulus K_1 and shear modulus μ_1, the spherical sheath formed by spheres of R_2 and R_1 represents a coating layer with K_2 and μ_2, and the sheath between spheres R_2 and R_3 the matrix with K_3 and μ_3. All constituent phases are supposed to be isotropic.

Table 1. Assumed Phase Properties[a]

	bulk modulus K [GPa]	shear modulus μ [GPa]
silica	40	30
solid polymer below T_g	4	$1 + i0.02$
polymer at T_g	$3.5(1 + i0.1)$	$0.01(1 + i)$
viscoelastic polymer above T_g	3	$0.001(1 + i0.1)$

[a] For silica, the moduli are real-valued and they are practically frequency independent. For the polymers, the assumed complex-valued moduli are typical of dynamic viscoelastic responses of organic polymers measured at commonly-employed laboratory frequencies, e.g., on the order of 1 Hz.

The effective medium is characterized by yet-unknown bulk modulus $K_4 = K_{\text{eff}}$ and shear modulus $\mu_4 = \mu_{\text{eff}}$. The whole system is subjected to a homogeneous deformation at infinity, and the effective moduli are determined self-consistently, by requiring that the average strain in the composite inclusion is the same as the macroscopic strain imposed at infinity (for more details, see the Appendix).

Historically, for a composite consisting of a dispersion of uncoated spheres in a matrix, the composite sphere model was introduced by Kerner.[8] The solution for the effective bulk modulus was straightforward. However, because of the algebraic complexity of the resulting equations, it took then a few decades to obtain exact solution for the effective shear modulus.[9] The generalized, n-layered composite-sphere model was subsequently formulated and solved by Herve and Zaoui.[10]

Results and Discussion

We first consider a model composite system consisting of nonlossy inclusions dispersed in a matrix with the same, nonlossy material properties as in the inclusions. The matrix and the inclusions are assumed to be separated by equal-thickness interfacial layers of a lossy viscoelastic material. For the matrix and inclusions, we took $K_1 = 3$ GPa and $\mu_1 = 1$ GPa while for the layer $K_1 = 3$ GPa and $\mu_2 = a(1 + i\eta)$ GPa, where a and η are two real-valued parameters. Perfect bonding is assumed at the interfaces. All calculations have been carried out assuming an angular frequency of $\omega = 1$ rad/s.

Figure 4 shows effective loss characteristics of such material, predicted numerically with a regular bcc model (open symbols) and a random Monte Carlo microstructure with 27 coated spheres (solid circles). In calculations, we assumed $a = 0.01$ GPa and $\eta = 0.5$—some typical values of a polymer in the glass transition region. Predictions of the four-phase sphere model are shown by solid lines. Remarkably, all three routes give very similar, practically indistinguishable predictions. This result is particularly arresting and important as at the volume fractions up to $f = 0.6$ studied here the elastic interactions between the neighboring spheres (particles) are obviously significant. We have already shown in our previous work that the corresponding three-phase composite sphere model was remarkably accurate at predicting the effective stiffness of sphere-reinforced composites.[11] Both three- and four-phase composite sphere models are self-consistent type models which account for the interactions between the particles in a mean-field, morphology-independent way. And their success indicates that the effective properties of composite materials with low-aspect-ratio inclusions are not particularly sensitive to the variations of local microstructures. In other words, the effective properties of such materials are predominantly determined by the volume fractions of the constituent phases. Alternatively, this result can be viewed as a direct manifestation of a more general finding that the representative volume element size in random-microstructure elastic composites is remarkably small.[2,12]

All in all, one concludes from the results presented in Figure 4 that the morphological effects are insignificant and that the coating layers of individual inclusions dissipate the energy practically independently. Therefore, when studying the effective properties of such systems one can rely on the predictions of the four-phase composite sphere model, which are definitely much easier to achieve than the finite element ones.

One can see from Figure 4 that the curves obtained at different volume fractions do not superimpose upon rescaling the loss modulus axis, thus indicating that at the volume fractions studied the overall responses are nonlinear functions of the inclusion volume fraction f. And this behavior should be expected in advance as at the volume fractions studied the elastic interactions between the inclusions are obviously quite significant. But surprisingly, the positions of the peaks stay practically independent of f, thus indicating that the underlying mechanisms (and hence the forms of local strains inside the layer sections predominantly contributing to the energy dissipation) remain the same at all the volume fractions studied.

Figure 5 presents the rates of local energy dissipation predicted with the four-phase sphere model. At infinity, harmonic strain $\boldsymbol{\varepsilon}_0 = \bar{\boldsymbol{\varepsilon}}_0 e^{i\omega t}$ was applied, with a frequency of $\omega = 1$ rad/s and with an amplitude tensor of

$$\bar{\boldsymbol{\varepsilon}}_0 = \begin{pmatrix} 1 & 0 & 0 \\ 0 & -1 & 0 \\ 0 & 0 & 0 \end{pmatrix} \tag{12}$$

Such strain tensor corresponds to a pure shear strain in a local frame rotated by 45 degrees around the z-axes. We have estimated complex-valued amplitudes of the local strain tensors in the sections of maximum energy dissipation (shown in red color in Figure 5). In the first peak at $\Delta/R \approx 0.2$ (where Δ and R are the thickness of the coating layer and the radius of the spheres, respectively), the strain tensor $\bar{\boldsymbol{\varepsilon}}_1$ turned out to be diagonal

$$\bar{\boldsymbol{\varepsilon}}_1 = \begin{pmatrix} \alpha_1 & 0 & 0 \\ 0 & \alpha_1 & 0 \\ 0 & 0 & \alpha_2 \end{pmatrix} \qquad \bar{\boldsymbol{\varepsilon}}_2 = \begin{pmatrix} \gamma & 0 & 0 \\ 0 & -\gamma & 0 \\ 0 & 0 & 0 \end{pmatrix} \tag{13}$$

whereas for the second peak at $\Delta/R \approx 0.007$ the strain tensor $\bar{\boldsymbol{\varepsilon}}_2$ had exactly the same form as that applied at infinity.

To understand the origin of the second peak, we have analyzed the asymptotic behavior for $a \to 0$. Figure 6 illustrates the results. One can see that both the maximum value and the shape of the second peak are independent of the absolute layer's stiffness a. Upon varying a, the second peak simply moves horizontally as a whole with a shift proportional to a, compare with eq 2. And the positions of the peaks obtained at different values of a also follow predictions of eq 2. All in all, the second peak has the same origin as the peak of μ_{eff} of lamellar systems; see Figure 1. The strain magnification γ at the second peak was quite significant, a factor of 50 at $a = 0.01$ GPa, and it scaled as $\gamma \sim 1/a$.

The three individual diagonal factors of $\bar{\boldsymbol{\varepsilon}}_1$ were of the order of unity, thus being significantly smaller than those observed in the second peak, see eq 13. Nonetheless, because of much larger Δ/R values, considerably larger volumes of the lossy layers were involved in the energy dissipation so the effective losses at the two peaks had comparable magnitudes. We have already discussed in the Introduction that upon loading of a lamella system perpendicular to the lamellas planes, it is the elastic constant C_{eff} which determines the energy dissipation, see Figure 1. We also saw that the maxima of C_{eff} and μ_{eff} occurred at different relative

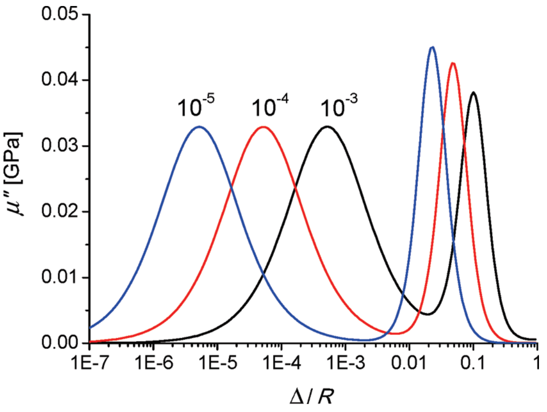

Figure 6. Predicted shifts of the loss peaks. In calculations, we assumed a nonlossy matrix and inclusions with identical bulk and shear moduli of $K = 3$ GPa and $\mu = 1$ GPa. For the coating layer, we assumed $K = 3$ GPa and $\mu = a(1 + i0.5)$ GPa and carried out calculations with the four-phase composite sphere model using three different values of absolute stiffness a shown in the figure.

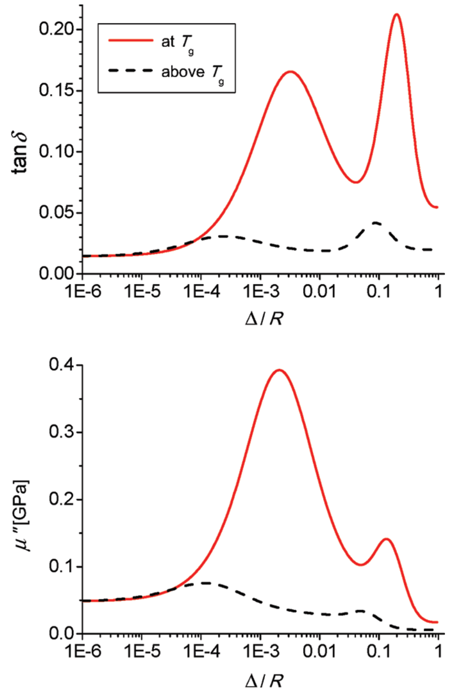

Figure 7. Predicted effective loss characteristics of a composite consisting of a dispersion of coated silica spheres in a solid polymer matrix. For the coating layers, the properties of either a polymer at T_g or a viscoelastic polymer well above T_g were assumed in calculations, see Table 1. The inclusion volume fraction was $f = 0.5$. The real part of the effective shear modulus (the stiffness) can be obtained via $\mu' = \mu''/\tan\delta$. In all the studies conducted in this work, the stiffness was a relatively flat, monotonously decreasing function of Δ. For definition of Δ and R, see the legend of Figure 4.

thicknesses of the lossy layer; see Figure 1. Equation 13 shows that at the two peaks, the local strain tensors occurring in the sections of maximum losses have a normal strain and pure shear form, respectively. Furthermore, Figure 5 shows that the maximum local energy dissipation rates observed at the two peaks occur in different sections of the coating layers. Accordingly, we relate the presence of the two peaks to two different, normal and shear modes of local deformations realizable inside the layers' sections determining the energy dissipation rates at the two peaks.

Experiments indicate that in the glass transition region, the bulk modulus also becomes lossy,[13] see Table 1. So we also conducted calculations assuming a nonzero bulk modulus of $K = 3.5(1 + i0.1)$ GPa. The resulting loss characteristics were practically indistinguishable from that shown in Figure 4. This result had to be expected for the second peak where the local strain in the sections of maximum energy dissipation had the same form as the externally applied strain. In the second peak, however, the strain tensor $\bar{\varepsilon}_1$ had a nonzero dilation part. However, the latter was in fact orders of magnitude smaller than the magnitudes of the individual factors α_i so it was again the shear part which determined the losses. We conclude that the coupling of volume and shear parts realizable in particulate morphology systems studied in this work is insufficient to influence the overall losses to any significant extent.

As an application, we considered a composite made up of a dispersion of coated silica inclusions in a solid polymer matrix. Stiff silica particles are fairly often used in practice to reinforce polymers. Typical rubber and glass-transition-region properties were assumed for the coating layers, see Table 1. Figure 7 presents results obtained assuming an inclusion volume fraction of $f = 0.5$. One can clearly see that the maximum losses are smaller than those seen with lamellar systems, see Figure 1. But nonetheless, the loss amplification in the second peak is still about a factor 20 or so compared to the loss modulus of the pure matrix. And the effective properties are now isotropic whereas for lamella systems they are usually strongly direction dependent. The losses can be further increased by increasing the inclusion volume fraction. But such systems may already be difficult to realize in practice. Interestingly, at the second peak at $\Delta/R \approx 0.005$ the volume fraction of the coating layers is very small, about 1% or so.

The effective loss modulus is getting considerably smaller upon increasing temperature moving away from the glass transition region of the layer material. But even with the coating layers operating in the viscoelastic domain above T_g, the effective shear loss modulus is comparable to that of pure polymers in their glass transition region where the shear loss modulus typically reaches values of 0.01−0.02 GPa. In fact, the values of effective loss modulus predicted at the second peak at around $\Delta/R \sim 10^{-4}$ are rather similar to those typical of carbon-black filled rubbers traditionally used in various acoustic and vibration damping applications.[14−19]

We have used the four-phase composite sphere model to generate results presented in Figure 7. For the coating layer and the matrix, we assumed some common material properties characteristic of polymers in three specific temperature regions, i.e., well below T_g, at around T_g and well above T_g, see Table 1. For reliability, we compared the model's predictions with the corresponding results of direct finite element calculations. And again, the agreement was very good, similar to the one seen in Figure 4. All in all, one can reliably use the four-phase composite sphere model to study the effective loss and stiffness characteristics of composite materials reinforced (or weakened) by a random dispersion of coated spheres. For example, one could readily use the model to predict the temperature dependence of the effective properties provided that the temperature dependence of the generally complex-valued viscoelastic phase properties is available.

In this work, we have conducted calculations assuming isotropic elastic behavior for all constituent phases. In practice, however, one should expect some confinement effects and preferred chain orientations inside thin coating layers and also in the vicinity of the interfaces between the constituent phases. These factors can certainly affect local stiffness and loss characteristics making them in general anisotropic and different from those typical of the bulk phases. To account for these factors would seriously complicate the exact treatment of the four-phase composite sphere model; see Appendix. From this perspective, the finite element route is advantageous, and one can readily use it to study such systems provided of course that the anisotropic phase moduli are available, either from experiments or from atomistic and/or mesoscopic simulations.

Conclusions

In this work, we have focused on particulate morphology materials and shown that the four-phase composite sphere model is remarkably accurate at predicting the effective properties of such systems. We demonstrated that by introducing thin layers of a viscoelastic material, one can significantly increase the loss characteristics of discrete morphology multiphase materials. Such lossy particulate−morphology materials may prove technologically appealing as one could use conventional polymer-processing equipment to directly process them into lossy complex-shape engineering parts suitable for various structural applications. Short fiber and continuous fiber reinforced materials commonly offer better reinforcing levels than those achievable with low aspect ratio inclusions at comparable loadings. It has already been shown that one can use the finite element route to extract reliable stiffness predictions for such composite materials.[20−23] We surmise that the general purpose time-domain finite element technique introduced in this work should also prove successful in studying and understanding the overall, effective viscoelastic properties of such materials.

Appendix: The Four-Sphere Composite Model

We use spherical coordinates with the origin at the center of the spheres; see Figure 3. As a general homogeneous deformation can be represented as a combination of a homogeneous hydrostatic dilatation (or compression) and a homogeneous shear, one can consider these two cases separately.

Pure Dilation θ_0 at Infinity. In this case, the displacement vector **u** is everywhere radial, and is a function of the radius-vector r alone. Therefore, the equation of equilibrium becomes **grad** div **u** = 0 . Hence

$$\operatorname{div} \mathbf{u} = \frac{1}{r^2}\frac{\mathrm{d}(r^2 u_r^{(i)})}{\mathrm{d}r} = \text{const} = 3a_i \tag{14}$$

or

$$u_r^{(i)} = a_i r + \frac{b_i}{r^2} \tag{15}$$

Here $u_r^{(i)}$ is the radial component of **u** in phase i. Coefficient b_1 must obviously vanish to avoid singularity at the origin while $a_4 = \theta_0/3$ to satisfy the boundary condition at infinity.

The radial stress in phase i is

$$\sigma_{rr}^{(i)} = 3K_i a_i - \frac{4\mu_i}{r^3} b_i \tag{16}$$

Where K_i and μ_i are the bulk and shear moduli of phase i, respectively.

To determine the unknown coefficients, one imposes the conditions of continuity of σ_{rr} and u_r at the three boundaries (interfaces) $r = R_i$ between phases i and $i+1$:

$$\sigma_{rr}^{(i)}(R_i) = \sigma_{rr}^{(i+1)}(R_i) \qquad u_r^{(i)}(R_i) = u_r^{(i+1)}(R_i) \tag{17}$$

For any effective medium with known moduli K_{eff} and μ_{eff}, one can solve the resulting six equations to obtain the six unknown coefficients. One can also use these equations to determine the effective moduli K_{eff} and μ_{eff} by requiring that the average dilatation in the composite inclusion is the same as the one imposed at infinity. This gives $b_4 = 0$ and also eliminates μ_{eff} from the list of unknown variables. Hence, one ends up with six equations for six unknown coefficients. By solving these equations, one determines both the effective bulk modulus K_{eff} and all the coefficients a_i and b_i.

Pure Shear γ_0 at Infinity. In this case, the displacement field in phase i is given by

$$\begin{cases} u_r^{(i)} = \left(A_i r - \dfrac{6\nu_i}{1-2\nu_i}B_i r^3 + 3\dfrac{C_i}{r^4} + \dfrac{5-4\nu_i}{1-2\nu_i}\dfrac{D_i}{r^2}\right)\sin^2\theta\cos 2\phi \\ u_\theta^{(i)} = \left(A_i r - \dfrac{7-4\nu_i}{1-2\nu_i}B_i r^3 - 2\dfrac{C_i}{r^4} + 2\dfrac{D_i}{r^2}\right)\sin\theta\cos\theta\cos 2\phi \\ u_\phi^{(i)} = -\left(A_i r - \dfrac{7-4\nu_i}{1-2\nu_i}B_i r^3 - 2\dfrac{C_i}{r^4} + 2\dfrac{D_i}{r^2}\right)\sin\theta\sin 2\phi \end{cases} \tag{18}$$

Here A_i, B_i, C_i, and D_i are unknown coefficients. Coefficients C_1 and D_1must vanish to avoid singularity at $r = 0$ while $B_4 = 0$ and $A_4 = \gamma_0$ to satisfy the boundary condition at infinity.

By imposing interface conditions for the displacement and stress components at $r = R_i$ and requiring that the average strain in the composite inclusion is the same as that applied at infinity, one obtains a system of twelve second order equations for eleven unknown coefficients of eq 18 plus the effective shear modulus $\mu_{\mathrm{eff}} = \mu_4$. By solving these equations, one determines both μ_{eff} and all the coefficients defining the underlying displacement field.

The resulting solutions for the effective bulk and shear moduli were presented elsewhere.[10] The final equations were given in a recurrent form so it would be rather difficult to write them here compactly. For more details, we refer the interested reader to the original work of Herve and Zaoui.[10]

References and Notes

(1) Jones, D. I. G. *Handbook of Viscoelastic Vibration Damping*; Wiley: Chichester, U.K., 2001.
(2) Gusev, A. A. *J. Mech. Phys. Solids* **1997**, *45*, 1449–1459.
(3) Gusev, A. A. *Macromolecules* **2001**, *34*, 3081–3093.
(4) Palmyra 2.4, MatSim GmbH: Zürich, Switzerland, http://www.matsim.ch.
(5) Gusev, A. A. *Phys. Rev. Lett.* **2004**, *93*, 034302.
(6) Zienkiewicz, O. C.; Taylor, R. L. *The Finite Element Method*, 5th ed.; Butterworth-Heinemann: Woburn, MA, 2000.
(7) Saad, Y. Iterative Methods for Sparse Linear Systems; PWS Publishing: Boston, MA, 1996.
(8) Kerner, E. H. *Proc. Phys. Soc. London* **1956**, *B69*, 808−813.
(9) Christensen, R. M.; Lo, K. H. *J. Mech. Phys. Solids* **1979**, *27*, 315–330.
(10) Herve, E.; Zaoui, A. *Int. J. Eng. Sci.* **1993**, *31*, 1–10.
(11) Gusev, A. A. *Adv. Eng. Mater.* **2007**, *9*, 117–120.
(12) Drugan, W. J.; Willis, J. R. *J. Mech. Phys. Solids* **1996**, *44*, 497–524.
(13) Ferry, J. D. *Viscoelastic Properties of Polymers*, 2nd ed.; Wiley: New York, 1970.
(14) Heinrich, G.; Klüppel, M. *Adv. Polym. Sci.* **2002**, *160*, 1–44.
(15) Heinrich, G.; Klüppel, M.; Vilgis, T. A. *Curr. Opin. Solid State Mater. Sci.* **2002**, *6*, 195–203.
(16) Berriot, J.; Montes, H.; Lequeux, F.; Long, D.; Sotta, P. *Macromolecules* **2002**, *35*, 9756–9762.
(17) Huber, G.; Vilgis, T. A. *Macromolecules* **2002**, *35*, 9204–9210.
(18) Gusev, A. A. *Macromolecules* **2006**, *39*, 5960–5962.
(19) Merabia, S.; Sotta, P.; Long, D. R. *Macromolecules* **2008**, *41*, 8252–8266.
(20) Gusev, A. A.; Hine, P. J.; Ward, I. M. *Compos. Sci. Technol.* **2000**, *60*, 535–541.
(21) Lusti, H. R.; Hine, P. J.; Gusev, A. A. *Compos. Sci. Technol.* **2002**, *62*, 1927–1934.
(22) Gusev, A. A.; Lusti, H. R.; Hine, P. J. *Adv. Eng. Mater.* **2002**, *4*, 927–931.
(23) Gusev, A. A.; Heggli, M.; Lusti, H. R.; Hine, P. J. *Adv. Eng. Mater.* **2002**, *4*, 931–933.